Catalysis Science & Technology

ROYAL SOCIETY OF CHEMISTRY

PAPER

View Article Online
View Journal | View Issue



Cite this: *Catal. Sci. Technol.*, 2025, 15, 5864

# Niobium oxide deposited on high surface area graphite as a stable catalyst in the 1-butanol dehydration reaction

J. M. Conesa, *[a] A. Guerrero-Ruiz, [bc] I. Rodríguez-Ramos [a] and M. V. Morales *[bc]

Niobium oxide, a promising catalyst for acid-catalyzed reactions in water-rich environments, often faces challenges due to its low specific surface area and performance highly dependent on synthesis conditions. In our study, niobium oxide was dispersed over a high-surface-area graphite support (HSAG), and the resulting composite catalysts were evaluated in the continuous gas-phase dehydration of 1-butanol under mild conditions (275 °C, atmospheric pressure). We systematically investigated the effects of the niobium precursor (chloride *vs.* oxalate), Nb loading (from 1/6 to 4/3 of the theoretical monolayer), and synthesis method—incipient wetness impregnation (IW) *vs.* urea-assisted deposition–precipitation (DP). Catalysts prepared by IW showed reduced surface areas and evidence of Nb oxide aggregation or partial reduction ($NbO_2$), while the DP method led to better dispersion, preservation of mesoporosity, and formation of orthorhombic $Nb_2O_5$, as revealed by X-ray photoelectron spectroscopy (XPS) and X-ray diffraction (XRD). Despite similar acid strength distributions, measured by ammonia temperature-programmed desorption (TPD-$NH_3$), catalytic stability varied markedly across samples. The DP catalyst exhibited outstanding stability and high selectivity toward $C_4$ olefins (≥90%), while IW catalysts experienced progressive deactivation. Post-reaction XRD confirmed structural stability, while thermogravimetric analyses coupled with mass spectroscopy (TGA-MS) revealed greater coke and isobutene retention—key deactivation factors—on deactivated IW samples. These findings demonstrate that the synthesis method governs catalyst dispersion, stability, and resistance to deactivation.

Received 22nd December 2024,
Accepted 13th August 2025

DOI: 10.1039/d4cy01531b

rsc.li/catalysis



## 1. Introduction

Due to their unique characteristics, niobium compounds and oxides find applications across various fields, including sensors[1] and solar cells.[2] Additionally, niobium's thermal and mechanical resilience enhances the durability of materials, and its versatility makes it valuable in the formulation of catalysts.[3,4] From this perspective, niobium displays unique properties not found in neighboring elements on the periodic table. These include high stability, strong oxygen affinity—leading to the formation of reactive surface species—and the ability to establish strong metal–support interactions.[3,4] Furthermore, niobium exhibits remarkable versatility in the oxides it can form, primarily appearing as NbO, $Nb_2O_3$, $NbO_2$, and $Nb_2O_5$, with the latter being the most thermodynamically stable. $Nb_2O_5$ may adopt various crystalline structures, with pseudohexagonal, orthorhombic, and monoclinic being the most common forms, listed in order of stability.[5,6] In its catalytic applications as an acidic solid, $Nb_2O_5$ is often utilized in its hydrated form, known as niobic acid ($H_2Nb_2O_6$). This material is an amorphous, water-insoluble solid composed of distorted $NbO_4$ tetrahedra and $NbO_6$ octahedra, similar to amorphous $Nb_2O_5$, and contains acidic protons within its structure.[7] This acidic solid possesses strong acidity, approximately 70% of that of $H_2SO_4$,[8] and can exhibit both Lewis and Brønsted acidic characters. Its appeal lies in the tunability of its acidic nature and the unique catalytic behavior of its acid sites, which is not observed in other acid catalysts with similar properties. The Brønsted acid sites present in the hydrated form of niobium pentoxide are attributed to the presence of surface hydroxyl (–OH) groups, primarily associated with the Nb–O bonds in distorted polyhedra and their connection points.[7] In contrast, Lewis acid sites are distributed within $NbO_4$ tetrahedra and can retain their functionality even in the presence of $H_2O$. These

[a] *Instituto de Catálisis y Petroleoquímica, CSIC, 28049, Madrid, Spain. E-mail: jm.conesa@csic.es*
[b] *Departamento de Química Inorgánica y Química Técnica, UNED, 28232, Las Rozas, Madrid, Spain. E-mail: mvmorales@ccia.uned.es*
[c] *Grupo de Diseño y Aplicación de Catalizadores Heterogéneos, Unidad Asociada al CSIC por el ICP, UNED, Madrid, Spain*

bonds are highly polarized and can fluctuate between Nb–OH and Nb═O configurations depending on proton abstraction.[9,10]

One of the most intriguing catalytic features of niobium oxides is the interaction and tolerance of their acidic sites with water molecules or protic compounds, such as alcohols. In the presence of water, niobium oxides exhibit a reversible transformation where Lewis acid sites convert into catalytically active Brønsted acid sites.[11] This transformation has been clearly observed in Brønsted acidity test reactions,[12] where introducing water enhances activity, unlike other solid acids, including metal oxides and zeolites. This behavior is particularly beneficial in biomass valorization reactions, such as esterification, which involves alcohols.[13] Moreover, while Lewis acid sites on metal oxides or zeolites are generally blocked by water adsorption, reducing catalytic activity, niobium oxides retain efficient acidic sites even after forming an acid–base adduct ($NbO_4$–$H_2O$) on the surface.[14] This feature is especially useful in aqueous-phase reactions, with successful results shown in processes such as glucose conversion to 5-hydroxymethylfurfural,[15] production of aromatics from lignin,[16] and the transformation of γ-valerolactone into pentanoic acid.[17]

Bioalcohols are essential biomass-derived compounds with substantial potential to replace petroleum derivatives, especially in challenging-to-decarbonize sectors.[18] Among short chain bioalcohols, bioethanol and biobutanol are particularly noteworthy due to their significant roles. While bioethanol remains the most widely produced bioalcohol, biobutanol is gaining importance in the sustainable fuel market because of its superior properties.[19–21] Known as *n*-butanol (hereafter referred to as BuOH), it is highly suitable as a direct fuel and valuable as a raw material for high-value products, owing to its higher carbon content.[2,22] The expected growth in biobutanol production demands efficient catalytic processes for its transformation, primarily through reactions that either retain or remove oxygen.[2,23] The dehydration of BuOH, besides releasing a water molecule, can proceed *via* two pathways (Scheme 1): (i) the intermolecular route, involving the condensation of two 1-butanol molecules forming DNBE (di-*n*-butyl ether) which may subsequently undergo the elimination of a BuOH molecule, resulting in the formation of the olefin 1-butene, and (ii) the intramolecular route through elimination of water from a single molecule, directly producing 1-butene. Generally, 1-butene readily isomerizes into a mixture of linear C4 olefins, or *n*-butenes, which have a well-established market for direct applications.[24,25] Moreover, these C4 olefins can be further oligomerized and hydrogenated to yield jet fuel-range hydrocarbons, potentially replacing jet fuel through the alcohol-to-jet (ATJ) pathway.[26,27]

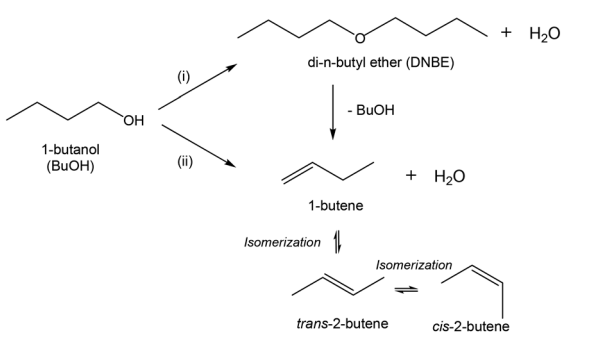


**Scheme 1** Reaction pathways for 1-butanol dehydration: (i) intermolecular dehydration and (ii) intramolecular dehydration.

The design of effective catalysts for BuOH dehydration reactions has focused on those predominantly containing either Lewis or Brønsted acid sites, with γ-$Al_2O_3$ (ref. 28–30) and the acidic zeolite H-ZSM-5 (ref. 31–36) serving as model catalysts, respectively. While catalysts with Lewis acid sites demonstrate substantial stability over reaction time, they typically require higher contact times and temperatures to achieve acceptable levels of selectivity and conversion.[37,38] However, these elevated temperatures lead to a decrease in selectivity toward butenes, as cracking reactions occur, resulting in the formation of lower molecular weight compounds such as methane, ethylene, or propylene.[39] Meanwhile, although catalysts with Brønsted acid sites exhibit significantly higher catalytic activity,[40,41] they often suffer from high deactivation rates and selectivity losses due to the occurrence of secondary reactions.[42] Catalyst deactivation, a key factor in sustainable butene production and somewhat related to the type of active site involved, is often underestimated in the research phase, yet it is crucial when designing and implementing a process, as it can determine its feasibility.[43]

In the search for alternative materials that can overcome the limitations associated with both Lewis and Brønsted acid site-based catalysts, niobium pentoxide has emerged as a promising candidate. A primary drawback of niobium oxide-based materials is their typically low specific surface area, which has driven extensive research efforts toward developing synthesis methods that produce mesoporous structures with enhanced surface exposure.[44,45] Additionally, supported niobium oxides exhibit highly variable catalytic behavior depending on the oxide loading. This variability gives rise to the formation of different polymeric species, which may generate catalytically active sites at the junctions between isolated species.[4,46]

Owing to the unique acidic properties and structural versatility of niobium oxides, catalysts derived from these materials show significant potential for application in BuOH dehydration reactions. Accordingly, this study presents catalytic results obtained by dispersing niobium oxide onto high-surface-area graphite (HSAG), evaluating the effects of oxide loading, as well as the influence of two different niobium precursor salts and two distinct synthesis methods.

## 2. Materials and methods

### 2.1. Catalyst synthesis

The HSAG ($S_{BET}$ = 396 $m^2$ $g^{-1}$) employed as a support was supplied by Timcal.

**2.1.1. Catalysts prepared by incipient wetness impregnation (IW).** The effect of the niobium oxide loading on the support was studied using niobium chloride ($NbCl_5$, Alfa Aesar, 99.95%) as a precursor, employing the IW method. The unit cell of $Nb_2O_5$ corresponds to a theoretical surface coverage of 6.3 Nb atoms per $nm^2$.[47,48] Catalysts were prepared using an appropriate solution volume with absolute ethanol as the solvent, achieving theoretical monolayer coverage values ranging from low levels, ensuring high dispersion (1/6 of the theoretical value), to values exceeding the theoretical monolayer (4/3), with intermediate levels of 1/3 and 2/3 of the theoretical monolayer. Secondly, a catalyst with a theoretical monolayer coverage of one-third (1/3) of the total was synthesized using the IW method and a niobium oxalate precursor salt ($Nb(HC_2O_4)_5$, Alfa Aesar). Due to the low solubility of niobium oxalate, a 0.1 M oxalic acid solution was used to completely dissolve the required amount of precursor salt.

**2.1.2. Catalyst prepared by the deposition–precipitation (DP) method.** Similarly, a catalyst with a theoretical niobium oxide content sufficient to cover 1/3 of the support surface was prepared using the DP method assisted by urea. Briefly, the required amount of niobium oxalate precursor salt was mixed with 250 mL of water in a round-bottom flask, and urea ($CH_4N_2O$) was added in a stoichiometric molar ratio of 2.5 (mol urea per mol Nb). The mixture was stirred vigorously, heated to 90 °C, and maintained under reflux for 17 h. Then it was filtered and repeatedly washed with distilled water. After synthesis, all materials were dried at room temperature for 12 h and then in an oven at 100 °C for 24 h and further calcined in static air at 400 °C for 4 h, following a heating program of 5 °C $min^{-1}$ from room temperature to 400 °C.

Table 1 provides a summary of the synthesized samples along with the nomenclature to be used, which specifies the theoretical monolayer percentage as well as the method and precursor used for each sample.

### 2.2. Catalyst characterization

The textural properties of the synthesized catalysts were evaluated by obtaining $N_2$ adsorption–desorption isotherms at liquid nitrogen temperature (−196 °C). The experiments were conducted using an ASAP2020 device (Micromeritics). Prior to measurement, the samples were degassed under vacuum at 150 °C for 16 hours. Given the mesoporous nature of the synthesized catalysts, the specific surface area was determined using the BET method. The total pore volume was estimated from the adsorbed amount at a relative pressure of 0.97, and the average pore size was calculated using the BJH method based on the desorption branch.

Thermogravimetric analyses (TGA) were carried out in an SDT Q 600 apparatus (TA Instruments) for both fresh (after thermal activation and pre-reaction) and spent catalysts (post-reaction), under inert (He, 100 mL $min^{-1}$) and air atmospheres (100 mL $min^{-1}$), respectively. The temperature program ranged from 30 °C to 800 °C (10 °C $min^{-1}$) and the evolution of the released gases was monitored using quadrupole mass spectrometry (Pfeiffer Vacuum Omnistar™ GSD 301).

Structural analysis of both fresh (before reaction) and spent catalysts (post-reaction) was carried out using X-ray diffraction (XRD) on a Polycrystal X'Pert Pro PANalytical diffractometer equipped with a copper anode X-ray source emitting characteristic Kα radiation ($\lambda$ = 0.1544 nm), operating at 45 kV and 40 mA. Bragg angles were measured between 4° and 90° at a step rate of 0.04° $s^{-1}$.

The dispersion of the niobium oxide domains over the HSAG support was studied by scanning transmission electron microscopy (STEM) by means of a JEOL JEM 3000F microscope operated at 300 kV and employing a spot size of 0.14 nm. X-ray energy dispersive spectroscopic (EDS) mapping analysis was performed with an ADF (GATAN) detector. The samples were ground and ultrasonically suspended in ethanol before microscopic analysis.

The electronic surface analysis and elemental surface composition measurements of the catalysts were conducted using X-ray photoelectron spectroscopy (XPS) on an Omicron spectrometer by SPECS, equipped with a PHOIBOS 100 R4 analyzer and an aluminum X-ray source (Kα = 1486.6 eV), operating at 75 W (12.5 kV and 6 A), with a pass energy of 30 eV and an energy step of 0.050 eV. Each sample was pressed into a small pellet, placed in the sample holder and degassed in the chamber for 6–8 h to achieve a dynamic vacuum below $10^{-8}$ Pa before analysis. Spectral analysis was performed using CASA XPS software, correcting the binding energy using the C(1s) signal from the aromatic ring of graphite at 284.6 eV.

**Table 1** Synthesis conditions, composition and textural properties of the synthesized catalysts

| Sample | Precursor | Nominal Nb weight (%) | Theorical Nb coverage (% monolayer) | Nb bulk content[a] (%) | BET surface area ($m^2$ $g^{-1}$) | Mesopore diameter (BJH)[b] (nm) | Pore volume ($cm^3$ $g^{-1}$) |
|---|---|---|---|---|---|---|---|
| HSAG | — | — | — | — | 396[c] | 5.7[c] | 0.47[c] |
| 1/6Nb(Cl)-IW | $NbCl_5$ | 6.1 | 16 | — | 240 | 4.3 | 0.30 |
| 1/3Nb(Cl)-IW | $NbCl_5$ | 11.5 | 33 | 12.6 | 219 | 3.9 | 0.22 |
| 2/3Nb(Cl)-IW | $NbCl_5$ | 20.6 | 66 | — | 201 | 3.3 | 0.18 |
| 4/3Nb(Cl)-IW | $NbCl_5$ | 34.1 | 133 | — | 165 | 3.2 | 0.13 |
| 1/3Nb(Ox)-IW | $Nb(HC_2O_4)_5$ | 11.5 | 33 | 10.1 | 205 | 4.3 | 0.17 |
| 1/3Nb(Ox)-DP | $Nb(HC_2O_4)_5$ | 11.5 | 33 | 9.0 | 356 | 6.4 | 0.42 |

[a] Determined by TGA in air considering that the final residue after complete carbon combustion corresponds to remaining $Nb_2O_5$. [b] BJH desorption average pore diameter. [c] Data reported in ref. 49.

 

The acidity of the catalysts was characterized by $NH_3$-TPD analysis, performed on a Micromeritics 2420 instrument. Approximately 100 mg of the sample was treated in a He flow at 350 °C to clean the catalyst surface before $NH_3$ chemisorption. $NH_3$ was adsorbed at 100 °C, and the catalyst was held under an inert atmosphere for 1 h to desorb weakly bound $NH_3$. The temperature was then ramped up at 10 °C $min^{-1}$ to 350 °C, with continuous $NH_3$ desorption monitoring, followed by isothermal conditions for 1 h.

### 2.3. BuOH dehydration reaction

Reaction tests were carried out using 150 mg of catalyst pre-calcined at 400 °C. Before testing, the catalysts were pressed and sieved to obtain grains between 0.35 mm and 0.55 mm, forming a catalytic bed with CSi. Prior to the introduction of 0.04 mL $min^{-1}$ of liquid BuOH into the reactor (using an HPLC pump), the catalytic bed was stabilized at the reaction temperature (275 °C) for 1 h. The gas products were analysed online by means of a gas chromatograph (450-GC) equipped with thermal conductivity (TCD) and flame ionization (FID) detectors. The compounds with high boiling points (BuOH and DNBE) were condensed and collected every reaction hour. These liquid samples were weighed and analysed using the same gas chromatograph, but in this case only the FID was used.

The butanol conversion ($X_{BuOH}$ (%)) and selectivity to product $i$ ($S_i$ (%)) were estimated employing the following equations, respectively:

$$X_{BuOH}\,(\%) = \frac{[F_{BuOH}]_{in} - [F_{BuOH}]_{out}}{[F_{BuOH}]_{in}} \cdot 100$$

$$S_i\,(\%) = \frac{n_i F_i}{[F_{BuOH}]_{in} - [F_{BuOH}]_{out}} \cdot 100$$

where $[F_{BuOH}]_{in}$ represents the molar flow of butanol fed to the reactor, $[F_{BuOH}]_{out}$ is the butanol molar flow at the reactor exit, $F_i$ is the molar flow of product $i$ (expressed in μmol $min^{-1}$) and $n_i$ is the stoichiometric factor of product $i$ relative to BuOH. The catalytic activity, per gram of catalyst or active phase ($m_{cat}$), is defined as:

$$\text{Catalytic activity}\left(\mu mol_{BuOH}\ min^{-1}\ g^{-1}\right) = \frac{X_{BuOH} \cdot [F_{BuOH}]_{in}}{100 \cdot m_{cat}}$$

The carbon mass balance CB (%) is determined as:

$$CB\,(\%) = \frac{\sum_i n_i F_i + [F_{BuOH}]_{out}}{[F_{BuOH}]_{in}} \cdot 100$$

## 3. Results and discussion

### 3.1. Textural and structural properties

Table 1 summarizes the textural parameters of the graphitic support and synthesized catalysts, and Fig. S1 shows the $N_2$ adsorption–desorption isotherms for the HSAG support and catalysts synthesized with niobium chloride. As observed, the isotherm of the HSAG support is type IVa (IUPAC) with an H3 hysteresis loop, typical of mesoporous materials formed by disordered graphitic layers. While the isotherm shape of the synthesized catalysts remained similar to that of HSAG, the specific surface area decreased significantly, from 396 $m^2\ g^{-1}$ for pristine HSAG to 165 $m^2\ g^{-1}$ for the catalyst with niobium content exceeding the theoretical monolayer. Even the lowest niobium-loaded catalyst shows a reduced surface area of 240 $m^2\ g^{-1}$. Despite these reductions, the catalysts retain high specific surface area, exceeding values reported for mesoporous niobium oxides in other studies.[17] As observed in Table 1, increasing niobium loading reduces surface area, pore size, and pore volume values. This is likely due to niobium oxide covering the edges of the graphitic layers, which contributes to mesoporosity, leading to reduced pore dimensions and volumes.[49] Fig. S2 shows the $N_2$ isotherms for catalysts with a theoretical coverage of 1/3 of the monolayer, synthesized by the two different methods (IW and DP), with niobium oxalate as the precursor. Interestingly, the synthesis *via* the DP method produces a material with significantly greater adsorption capacity compared to the IW method, resulting in an enhanced specific surface area and pore volume (1/3Nb(Ox)-DP). It is important to note that the HSAG used as a support is a lamellar material whose mesoporosity arises mainly from interparticle voids rather than from interlayer spacing or intrinsic microporosity. No exfoliation or expansion of the graphite layers is expected, as no intercalating agents or high-energy treatments were applied during synthesis. Hence, the higher surface area of the DP sample is most likely due to the preservation of the interparticle porosity. In the IW method, the concentrated precursor solution can lead to localized deposition and partial pore blockage between graphite particles, thus reducing both surface area and pore volume. In contrast, the urea-assisted deposition–precipitation route promotes gradual and homogeneous deposition of niobium species, minimizing obstruction and allowing better access to the existing porous network of the HSAG support.

The strong affinity of niobium for oxygen facilitates the decomposition of its precursors and the subsequent formation of niobium oxide at the calcination temperature (400 °C).[50] This is supported by gas evolution analysis during thermal treatment under an inert atmosphere, as exemplified in Fig. S3 for the 2/3Nb(Cl)-IW sample. In the fresh material, mass spectrometric signals corresponding to chlorinated species ($m/z$ = 36) appear at around 200 °C, indicating precursor decomposition. These signals disappear in the sample obtained after calcination in air at 400 °C for 4 hours and remain absent up to the maximum temperature tested (800 °C), confirming the complete removal of chlorine. This behaviour was consistently observed in all catalysts synthesized using niobium chloride as the precursor.

Thermogravimetric analysis under an air atmosphere, performed after the activation treatment, provides an

estimate of the niobium oxide content in the catalysts. Assuming full combustion of the carbon support and that the residue consists entirely of $Nb_2O_5$, the measured niobium content is consistent across the catalysts and close to the theoretical value, enabling a direct comparison of their catalytic behaviour. As shown in Fig. S4 and collected in Table 1, the final weights for the samples with a nominal loading corresponding to 1/3 of a monolayer are similar and closely match the theoretical $Nb_2O_5$ content of 11.5%, with minor deviations due to physisorbed water. The slightly higher niobium oxide content for 1/3Nb(Cl)-IW (12.6%) is attributed to partial decomposition of the chloride precursor in ambient moisture. In contrast, the oxalate precursor (1/3Nb(Ox)-IW) provides niobium content closer to theoretical levels (10.1%), while the DP method (1/3Nb(Ox)-DP) may not fully incorporate all niobium from the solution (9.0%).

The structural study of the catalysts after activation treatment *via* XRD (Fig. 1) reveals significant differences between the samples. In addition to the characteristic diffraction peaks of the HSAG support, including a pronounced peak at $2\theta \approx 26°$, corresponding to the (002) reflection plane of graphite, the incorporation of niobium species generates low-intensity signals attributed to $NbO_2$ species, whose intensity is more perceptible in the high loaded samples but is absent in the catalyst synthesized by DP. Despite the lower stability of $NbO_2$ compared to $Nb_2O_5$ and the lack of such species in similar treatments on silica,[50] their stabilization can be attributed to the reducing nature of the carbonaceous support. Carbon materials are well-known for their ability to reduce metals at high temperatures, often facilitating the formation of niobium carbides starting from intermediate oxidation states.[51] These species can appear at relatively low temperatures,[52] although higher temperatures are typically required when working with bulk niobium oxide materials. In contrast, the diffractogram of the sample synthesized by deposition–precipitation (1/3Nb(Ox)-DP) shows distinct, albeit low intensity, signals. Notably, the peak corresponding to the (001) plane of the orthorhombic $Nb_2O_5$ structure (PDF 30-0873) appears at $2\theta \approx 22°$. These diffraction signals are absent in the catalysts synthesized by IW, further highlighting differences in the crystallinity and dispersion of niobium species between the two synthesis methods.

Additional insight into the morphology and surface distribution of the niobium species was obtained by STEM. Although the resolution of the acquired micrographs limits detailed structural interpretation, qualitative trends are apparent among the four samples analyzed (Fig. S5). The catalyst prepared *via* deposition–precipitation (1/3Nb(Ox)-DP) exhibits well-defined, individual particles with a distinguishable morphology, contrasting with the more diffuse, plate-like features observed in the IW-prepared catalysts. These features are consistent with the higher BET surface area of this sample (Table 1) and suggest a discrete and homogeneous dispersion of niobium oxide domains. Elemental mapping analysis (Fig. S6) further supports this interpretation, revealing a uniform distribution of niobium and oxygen over the support surface, in agreement with XPS data showing the highest surface Nb/C ratio among the series (Table 2). In contrast, the 1/3Nb(Cl)-IW and 1/3Nb(Ox)-IW samples display broader, less defined regions, where the graphite support appears to be partially coated by overlapping lamellar structures (Fig. S5).

While the 1/3Nb(Ox)-IW catalyst shows a more heterogeneous texture with local contrast variations, possibly related to localized Nb aggregation, the Cl-based IW sample appears to be more uniformly coated. The most extensive surface coverage is observed for the 2/3Nb(Cl)-IW catalyst, in which the graphite substrate is almost entirely hidden, consistent with the higher surface Nb content measured by XPS, as discussed below (Table 2).

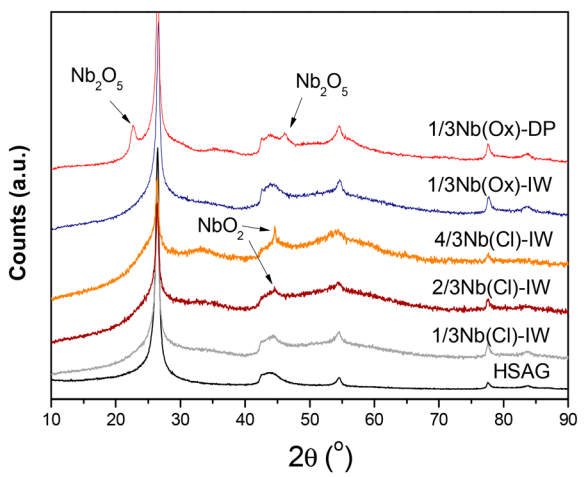


Fig. 1 XRD patterns of supported niobium catalysts after thermal treatment.

### 3.2. Surface properties

The electronic properties of the synthesized catalysts were studied using XPS and the dispersion of niobium species on the support was determined by calculating the surface atomic ratio of Nb to C, collected in Table 2 and represented in Fig. 2, *vs.* the $Nb_2O_5$ content. It is observed that the surface

Table 2 Surface properties of the support and catalysts

| Sample | Atomic surface content[a] (%) | | | Nb/C ratio[a] ($\times 10^3$) | Total acid sites[b] (mmol $g^{-1}$) |
|---|---|---|---|---|---|
| | C | Nb | O | | |
| HSAG | 95.1 | — | 4.9 | — | 0.12 |
| 1/6Nb(Cl)-IW | 91.0 | 0.7 | 8.3 | 7.6 | 0.14 |
| 1/3Nb(Cl)-IW | 86.6 | 1.0 | 12.4 | 11.8 | 0.19 |
| 2/3Nb(Cl)-IW | 81.2 | 3.4 | 15.3 | 42.3 | 0.25 |
| 4/3Nb(Cl)-IW | 72.9 | 5.7 | 21.4 | 78.3 | 0.27 |
| 1/3Nb(Ox)-IW | 91.1 | 0.7 | 8.1 | 7.8 | — |
| 1/3Nb(Ox)-DP | 86.6 | 2.0 | 11.4 | 22.7 | 0.24 |

[a] Determined by XPS measurements. [b] Obtained by $NH_3$-TPD analysis.

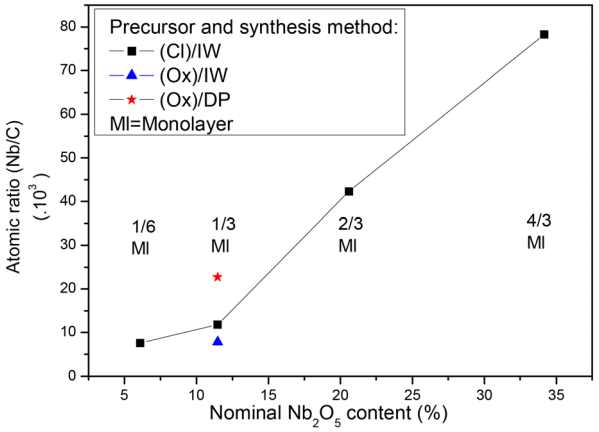


**Fig. 2** Atomic Nb/C ratio determined by XPS as a function of the incorporated $Nb_2O_5$ percentage.

Nb/C ratio increases proportionally with the $Nb_2O_5$ content for catalysts 1/6Nb(Cl)-IW and 1/3Nb(Cl)-IW; however, for catalysts with higher Nb loading, the increase in Nb/C ratio exceeds expectations. The catalyst synthesized by DP shows a higher relative surface niobium content, indicative of greater dispersion, compared to its IW counterpart with the chloride precursor. Additionally, the IW catalyst prepared with the niobium oxalate precursor exhibits the lowest surface niobium content among the series, suggesting a poorer dispersion. These trends detected by XPS are in line with those observed in the STEM images. In contrast, the 2/3Nb(Cl)-IW catalyst, whose STEM image revealed almost complete coverage of the carbon support, presented a sharp increase in surface Nb concentration.

Hence, key conclusions from the semiquantitative XPS analysis are as follows: (i) the surface Nb content gradually increases with the bulk $Nb_2O_5$ loading but does not plateau, indicating incomplete surface saturation, (ii) the increase in Nb loading from 1/3 to 2/3 monolayer leads to a significant rise in the Nb/C ratio, consistent with the observed reduction in surface area, (iii) niobium does not form atomically thin layers but is well-dispersed on the support, as evidenced by the higher dispersion achieved with the DP method, and (iv) the absence of a plateau despite high niobium loadings suggests small, low-crystallinity niobium oxide particles, corroborating the XRD results. These combined results confirm that synthesis *via* DP leads to better-dispersed niobium species, while IW—especially at higher loadings—promotes aggregation and partial reduction of the oxide phase.

The accumulated XPS spectra in the binding energy range corresponding to the Nb 3d region reveals slight differences depending on the synthesis method (Fig. 3). All the catalysts exhibit the characteristic Nb 3d doublet with a separation of 2.72 eV, consistent with oxidized niobium species. The peak centered at around 207.6 eV, present in the 1/3Nb(Cl)-IW (Fig. 3a), 1/3Nb(Ox)-IW (Fig. 3b) and 1/3Nb(Ox)-DP (Fig. 3c) samples, is attributed to the $3d_{5/2}$ orbital of $Nb^{5+}$,[53] while the lower binding energies observed in the 2/3Nb(Cl)-IW sample

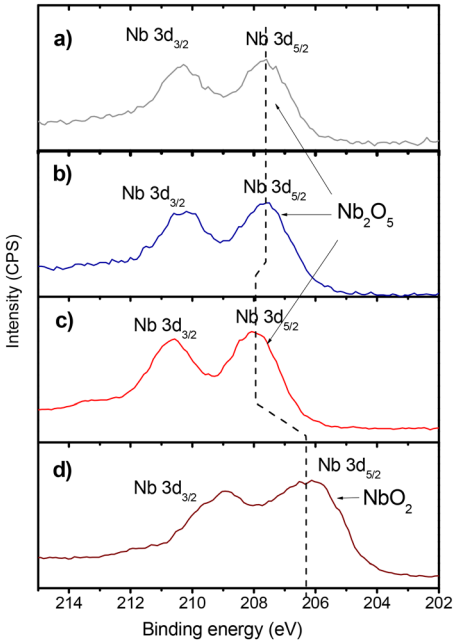


**Fig. 3** XPS spectra in the Nb 3d region: a) 1/3Nb(Cl)-IW, b) 1/3Nb(Ox)-IW, c) 1/3Nb(Ox)-DP and d) 2/3Nb(Cl)-IW.

(Fig. 3d), correspond to $NbO_2$ species, typically ranging from 206.8 to 207.3 eV.[53–55] When comparing the three catalysts with 1/3 monolayer coverage, it is interesting to note that the DP-synthesized sample (Fig. 3c) shows a slight shift to higher binding energies and narrower peaks, indicating more electron-deficient, oxidized niobium.

The deconvolution of the O 1s XPS spectra (Fig. S7) further supports the differences in niobium oxide dispersion and the chemical state among catalysts. On the one hand, among the three catalysts with identical theoretical Nb loading (1/3 monolayer), the O 1s signal at ~531.0 eV—assigned to lattice oxygen in $Nb_2O_5$—is significantly more intense in the 1/3Nb(Ox)-DP catalyst than in the IW-prepared counterparts. This difference strongly suggests a higher surface concentration and dispersion of niobium oxide species in the DP sample, which correlates with the higher Nb/C surface ratio and supports the conclusion that the DP method enhances the accessibility and distribution of the active phase. On the other hand, the presence of $NbO_2$ observed in the Nb 3d region in the higher loaded sample (2/3Nb(Cl)-IW) is further supported by the O 1s spectra of this sample (Fig. S7), where the main component appears to be significantly shifted to a lower binding energy (~530.0 eV), in contrast to the 1/3Nb samples (530.9–531.0 eV). The shift in O 1s is characteristic of oxygen bound to partially reduced niobium species. This interpretation aligns well with the XRD results, where low-intensity reflections attributed to $NbO_2$ phases were observed (Fig. 1).

The acidity of the catalysts was evaluated by TPD-$NH_3$, and the results are shown in Fig. 4 and Table 2. As exposed in the Introduction section, niobium oxide can exhibit both

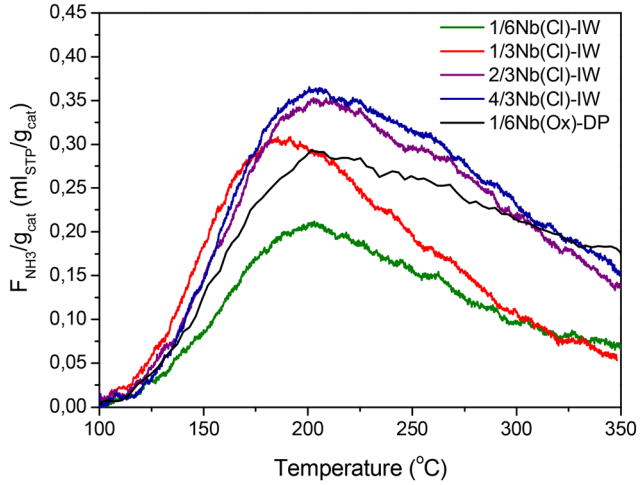


Fig. 4 TPD-$NH_3$ curves of Nb-supported catalysts.

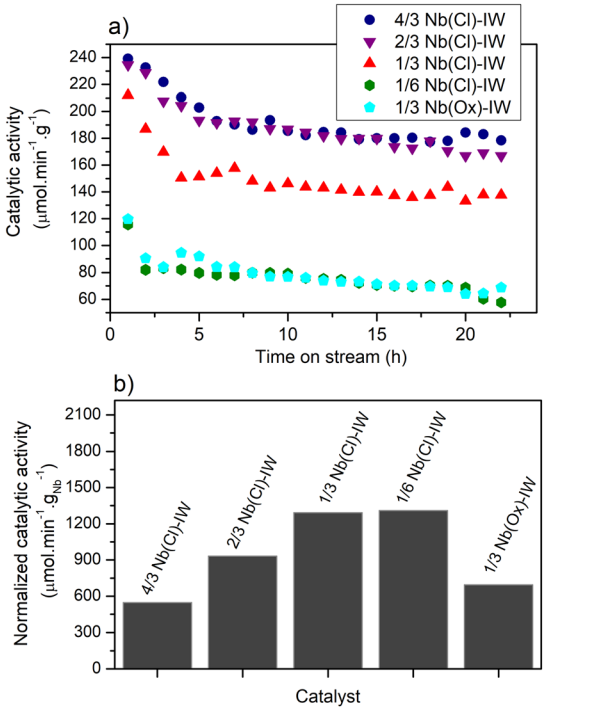


Fig. 5 Catalytic activity of IW-synthesized catalysts, expressed per gram of catalyst (a) and per gram of incorporated niobium after 8 h on stream (b). Reaction conditions: $T$ = 275 °C; $F_{(He)}$ = 100 ml min$^{-1}$; $P_{(BuOH)}$ = 9.78 kPa; $W_{cat}$ = 150 mg.

Lewis and Brønsted acid sites, in the form of Nb=O bonds and Nb–OH groups, respectively.[9,10] Although TPD-$NH_3$ analysis does not permit discrimination between Brønsted and Lewis sites, the amount of desorbed $NH_3$ is an indirect measure of the material overall acidity. The parent HSAG support exhibits a low acidity (0.12 mmol g$^{-1}$, Fig. S8), attributed to surface functionalities inherent to the carbonaceous material. Upon deposition of niobium oxide, all the catalysts show an increase in acidity, confirming the generation of new acid sites associated with the niobium species. The desorption profiles exhibit broad peaks centered at around 200 °C, indicative of weak to medium-strength acid sites, with no significant contribution from strongly acidic sites at higher temperatures. As shown in Table 2, the total acidity increases with niobium loading in the IW series, from 0.14 mmol g$^{-1}$ for 1/6Nb(Cl)-IW to 0.27 mmol g$^{-1}$ for 4/3Nb(Cl)-IW. This trend is consistent with the increasing surface Nb/C ratio determined by XPS, suggesting that niobium species contribute directly to the formation of accessible acid sites. The 1/3Nb(Ox)-DP sample displays a total acidity of 0.24 mmol g$^{-1}$, higher than its IW counterpart with the same nominal loading (0.19 mmol g$^{-1}$). This enhanced acidity may be related to better niobium dispersion, as previously discussed, which allows a greater fraction of Nb sites to be accessible and active.

### 3.3. Catalytic performance in the 1-butanol dehydration reaction

The niobium oxide supported samples were evaluated in the 1-butanol dehydration reaction at 275 °C. Before initiating the catalytic evaluations, the absence of catalytic activity was confirmed in both the blank and HSAG support experiments.

**3.3.1. Effect of Nb loading on catalytic activity.** Fig. 5a shows the catalytic activity per gram of catalyst as a function of time on stream for the series of IW-synthesized catalysts with varying niobium loadings. Among the catalysts prepared using the chloride precursor, an increase in activity is observed with increasing theoretical monolayer coverage, up to 2/3. However, the 4/3 monolayer sample does not follow this trend, showing a similar activity to the 2/3 sample despite the higher nominal loading. All the catalysts exhibit a marked initial deactivation that stabilizes over time, a behavior commonly reported for this reaction.[49,56] Notably, the extent of deactivation is more pronounced in the initially more active catalysts.

A clearer picture of niobium utilization efficiency emerges when the activity is normalized per gram of incorporated niobium (Fig. 5b). Under these conditions, the catalysts with 1/6 and 1/3 monolayer coverage display nearly identical activity, whereas further increases in Nb loading result in a decline in normalized activity. This suggests that, beyond a certain loading, additional niobium species do not contribute proportionally to the catalytic performance, likely due to lower dispersion or pore blocking, as indicated by the decrease in BET surface area and the emergence of $NbO_2$ species in XRD and XPS at higher loadings. The TPD-$NH_3$ data also show that acidity increases with Nb content, but this does not translate into higher catalytic efficiency. Therefore, 1/3 of the theoretical monolayer is identified as the optimal Nb loading under the present synthesis conditions.

**3.3.2. Effect of the precursor and synthesis method on catalytic activity and stability.** With the optimal loading of 1/3 of the theoretical monolayer in mind, this composition was selected to compare the effect of the niobium

 

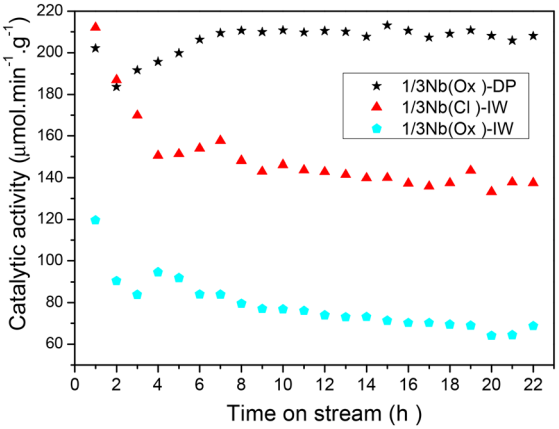


**Fig. 6** Catalytic activity over reaction time for catalysts synthesized with a theoretical monolayer coverage of 1/3. Reaction conditions: $T$ = 275 °C; $F_{(He)}$ = 100 ml min$^{-1}$; $P_{(BuOH)}$ = 9.78 kPa; $W_{cat}$ = 150 mg.

precursor and synthesis method on catalytic performance (Fig. 6). Among the IW-synthesized catalysts, the sample prepared from niobium oxalate (1/3Nb(Ox)-IW) exhibited slightly lower catalytic activity than its chloride-based counterpart (1/3Nb(Cl)-IW). Both IW catalysts showed a pronounced initial deactivation followed by a slower decline in activity, which is typical in butanol dehydration reactions due to coke formation or active site blockage.[23,39]

In contrast, the catalyst prepared by DP (1/3Nb(Ox)-DP) demonstrated remarkable stability, maintaining a nearly constant activity over the full 22-hour time-on-stream period. This behavior stands out for a reaction that is known to be strongly influenced by acidity and prone to deactivation. The enhanced performance of the DP catalyst can be rationalized based on its physicochemical properties. It presents a higher BET surface area and a more uniform dispersion of niobium species, as evidenced by XPS and STEM. Moreover, XRD analysis indicates the presence of the orthorhombic $Nb_2O_5$ phase, known for its water-tolerant and catalytically robust nature, which may further contribute to the observed long-term stability.[5] The textural and surface characterization of the IW-prepared catalysts, on the other hand, showed reduced surface areas and signs of partial pore blockage, pointing to less accessible and potentially more heterogeneous active phases. $NH_3$-TPD analysis supports this interpretation: although total acidity increases with Nb loading, all the samples show similar acid strength distributions. The DP catalyst, with lower total niobium content but higher dispersion, provides a more effective and accessible distribution of acid sites, enabling sustained catalytic performance.

The decline in catalytic activity observed for the IW-prepared catalysts, particularly 1/3Nb(Cl)-IW, can be further understood in light of the post-reaction characterization. The XRD patterns recorded after the reaction show no significant structural changes in any of the catalysts, ruling out bulk phase transformation or collapse as the cause of deactivation (Fig. S9). However, thermogravimetric analysis coupled with mass spectrometry (TGA-MS) provides clear evidence of surface carbon accumulation (Fig. S10). When comparing the fresh and spent catalysts, a distinct weight loss starting from 200 °C up to around 400 °C is observed in the post-reaction samples—absent in the fresh materials—indicating the oxidation of coke deposits, confirmed by the detection of the $m/z$ = 44 fragment by MS analysis. This weight loss is especially pronounced for 1/3Nb(Cl)-IW, suggesting a greater extent of carbon buildup on this catalyst.

Although some carbon accumulation is also detected on the DP catalyst, it is significantly lower in intensity. MS analysis of the desorbed fragments provides additional insight into the chemical nature of these residues (Fig. S11). In particular, signals at $m/z$ = 56 correspond to the molecular ion of $C_4$ olefins ($C_4H_8^+$), common to all isomers (1-butene, *cis*-2-butene, *trans*-2-butene, isobutene), while $m/z$ = 41 corresponds to a characteristic fragment ion ($C_3H_5^+$), whose relative intensity varies between isomers. Notably, isobutene, due to its branched structure, generates more $m/z$ = 41 fragments, leading to a higher 41/56 ratio than linear isomers like 2-butene. In the case of the 1/3Nb(Cl)-IW catalyst, the observed 41/56 ratio (2.24) is significantly higher than the ratio found in the DP catalyst (1.74), suggesting that isobutene is more strongly retained and/or prone to oligomerization[57] on the IW-prepared surface. These findings reinforce the idea that the DP method not only ensures better niobium dispersion and acid site accessibility, but also mitigates deactivation by minimizing coke precursors and facilitating their removal.

**3.3.3. Product distribution and reaction mechanism.** The product distribution obtained over catalysts with 1/3 of the theoretical monolayer is represented in Fig. 7. It should be noted that all catalytic tests were conducted under differential conditions (conversions maintained below 10%) specifically to ensure that initial activities and selectivities

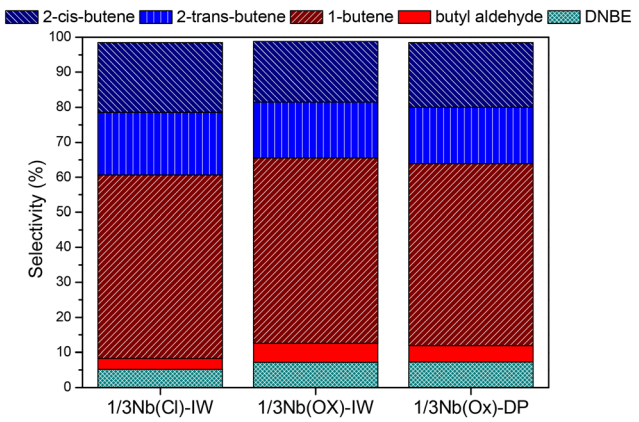


**Fig. 7** Product distribution obtained over catalysts synthesized with a theoretical monolayer coverage of 1/3. Reaction conditions: 2 h reaction time, $T$ = 275 °C; $F_{(He)}$ = 100 ml min$^{-1}$; $P_{(BuOH)}$ = 9.78 kPa; $W_{cat}$ = 150 mg. Selectivity values obtained at differential conversion levels: 6.43% for 1/3Nb(Cl)-IW, 3.10% for 1/3Nb(Ox)-IW and 6.30% for 1/3Nb(Ox)-DP.

could be directly compared across catalysts without the influence of secondary reactions. Nevertheless, the best-performing catalyst (1/3Nb(Ox)-DP) was tested at higher conversion levels (~30%, not shown for the sake of brevity), and it was observed that both product distribution and catalyst stability remained unchanged, confirming that the reported selectivities are representative and robust across a broader range of conversions.

As shown in Fig. 7, all the catalysts evaluated after 2 hours on stream exhibit high selectivity toward $C_4$ olefins (≥90%), indicating that intramolecular dehydration is the dominant reaction pathway under the conditions employed (see Scheme 1). This mechanism is typically favored at moderate temperatures and proceeds *via* both Brønsted and Lewis acid sites, which facilitate the elimination of the hydroxyl group. In the Brønsted acid-catalyzed route, the alcohol OH group is protonated, promoting its departure and enabling the formation of a C=C double bond through β-elimination. In contrast, Lewis acid sites act as electron acceptors, polarizing the C–O bond and inducing its cleavage, thereby generating the alkene while hydroxylating the catalytic surface. The resulting OH group can then recombine with a β-proton to form water, completing the catalytic cycle.

The major products detected in all cases were 1-butene and its *cis*- and *trans*-2-butene isomers, with *cis*/*trans* ratios close to unity. This distribution is typical of moderately acidic environments,[58] and suggests that the catalysts possess acid sites of sufficient strength to promote isomerization, but not so strong as to induce significant secondary reactions such as cracking. This interpretation aligns with the TPD-$NH_3$ profiles, which show broad desorption bands centered at around 200–250 °C, indicative of weak to medium-strength acid sites. The similar shape of the desorption profiles, despite variations in total acidity, suggests comparable acid strength distributions across all catalysts.

Minor amounts of DNBE obtained from the intermolecular route (Scheme 1) were detected in all samples, slightly more pronounced in the IW-prepared catalysts. Trace levels of butyraldehyde, resulting from dehydrogenation pathways, were also observed but were negligible, confirming the selectivity of the system toward dehydration. Interestingly, the consistently high $C_4$ olefin selectivity across all the samples—regardless of the precursor or synthesis method—suggests that all the catalysts maintain active acidic functionalities, even though their accessibility and dispersion, which differ significantly as shown by surface and structural characterization, impact their overall activity and stability.

It is worth noting that carbon balances exceeded 95% in all cases, confirming the robustness of the experimental protocol and the accurate quantification of both gas-phase and condensed-phase products. This high closure also indicates that undesired side reactions such as cracking to light hydrocarbons or coke formation were minimal under the operating conditions. The absence of significant carbon loss further supports the conclusion that the observed differences in catalytic performance stem from intrinsic textural and surface properties, not from degradation or instability of the materials.

# 4. Conclusions

This work reports the development of niobium oxide-based catalysts supported on HSAG for the gas-phase dehydration of 1-butanol. To maximize the exposure of active sites, $Nb_2O_5$ was dispersed on the HSAG surface, and the effects of niobium loading—from a submonolayer (1/6) to a supermonolayer (4/3)—were systematically studied. Two niobium precursors (niobium chloride and niobium oxalate) and two synthesis methods (incipient wetness impregnation, IW, and urea-assisted deposition–precipitation, DP) were compared to evaluate their influence on the catalyst structure, surface properties, and catalytic behavior.

All the catalysts showed high selectivity toward intramolecular dehydration products (*n*-butenes), with minor amounts of DNBE and butyraldehyde as by-products. The product distribution was consistent with a mechanism dominated by medium-strength Brønsted and Lewis acid sites. An optimal niobium loading of 1/3 monolayer was identified based on the catalytic activity normalized per gram of catalyst and per gram of niobium. Higher loadings did not enhance performance, likely due to reduced dispersion and partial blocking of interparticle porosity. $NH_3$-TPD analysis showed that the acid strength remained similar across samples, indicating that differences in activity and stability are mainly driven by acid site density and accessibility, not intrinsic acidity.

The synthesis method was found to be a critical factor. The IW catalysts displayed reduced surface area, signs of pore blockage, and formation of partially reduced niobium species (*e.g.*, $NbO_2$), especially at higher loadings. In contrast, the DP catalyst retained the surface area of the support, showed well-dispersed niobium species in the orthorhombic $Nb_2O_5$ phase (revealed by XRD and XPS), and exhibited superior stability under reaction conditions. This was further confirmed by post-reaction XRD, which showed no structural degradation, and by TGA-MS, which revealed significantly lower coke accumulation on the DP sample. Mass spectrometric analysis of desorbed fragments further indicated a higher retention of isobutene—a known coke precursor—on the deactivated IW sample.

In summary, niobium oxide catalysts supported on HSAG, especially that synthesized by the DP method, offer a promising platform for biobutanol valorization *via* selective and stable dehydration. These materials provide valuable insights for designing acid catalysts with tunable dispersion and surface chemistry, potentially extendable to other oxygenated bio-derived feedstocks.

# Author contributions

J. M. Conesa: conceptualization, methodology, investigation, writing – original draft. I. Rodríguez-Ramos: supervision,

 

project administration, funding acquisition. A. Guerrero-Ruiz: supervision. M. V. Morales: data curation, supervision, writing – original draft, writing – review & editing. All authors have given approval to the final version of the manuscript.

## Conflicts of interest

There are no conflicts to declare.

## Data availability

Supplementary information is available. See DOI: **https://doi.org/10.1039/D4CY01531B**.

The data supporting this article have been included as part of the SI. The SI provides additional characterization data ($N_2$ adsorption–desorption, TG-DTG/MS, STEM-EDX, XPS, $NH_3$-TPD, XRD of spent catalysts) supporting the discussion of textural, structural and catalytic stability. Further data are available upon request from the authors.

## Acknowledgements

This work was supported by the project PID2023-146481OB-I00 funded by MICIU/AEI/10.13039/501100011033 and FEDER/UE. J. M. Conesa gratefully acknowledges the funding provided by UNED to carry out his Ph.D. (EIDUNED; jconesa61@alumno.uned.es). M. V. Morales acknowledges the funding received through the "Ramón y Cajal 2022" program (RYC2022-036981-I). The authors acknowledge the Universidad Complutense de Madrid (ICTS-Centro Nacional de Microscopía Electrónica) for supporting us with the STEM-EDX analysis.

## References

1 H. Liu, N. Gao, M. Liao and X. Fang, Hexagonal-like $Nb_2O_5$ Nanoplates-Based Photodetectors and Photocatalyst with High Performances, *Sci. Rep.*, 2015, **5**(1), 7716.
2 M. Lira-Cantu, K. Norrman, J. W. Andreasen and F. C. Krebs, Oxygen Release and Exchange in Niobium Oxide MEHPPV Hybrid Solar Cells, *Chem. Mater.*, 2006, **18**(24), 5684–5690.
3 K. Tanabe, Catalytic application of niobium compounds, *Catal. Today*, 2003, **78**(1–4), 65–77.
4 M. Ziolek, Niobium-containing catalysts—the state of the art, *Catal. Today*, 2003, **78**(1), 47–64.
5 Y. Zhao, X. Zhou, L. Ye and S. Chi Edman Tsang, Nanostructured $Nb_2O_5$ catalysts, *Nano Rev.*, 2012, **3**(1), 17631.
6 C. Nico, T. Monteiro and M. P. F. Graça, Niobium oxides and niobates physical properties: Review and prospects, *Prog. Mater. Sci.*, 2016, **80**, 1–37.
7 S. Kang, R. Miao, J. Guo and J. Fu, Sustainable production of fuels and chemicals from biomass over niobium based catalysts: A review, *Catal. Today*, 2021, **374**, 61–76.
8 K. Tanabe, Catalytic application of niobium compounds, *Catal. Today*, 2003, **78**(1–4), 65–77.
9 S. M. Maurer and E. I. Ko, Structural and acidic characterization of niobia aerogels, *J. Catal.*, 1992, **135**(1), 125–134.
10 J. M. Jehng and I. E. Wachs, Molecular structures of supported niobium oxide catalysts under in situ conditions, *J. Phys. Chem.*, 1991, **95**(19), 7373–7379.
11 K. Omata and T. Nambu, Catalysis of water molecules acting as Brönsted acids at Lewis acid sites on niobium oxide, *Appl. Catal., A*, 2020, **607**, 117812.
12 Q.-L. Dai, B. Yan, Y. Liang and B.-Q. Xu, Water effects on the acidic property of typical solid acid catalysts by 3,3-dimethylbut-1-ene isomerization and 2-propanol dehydration reactions, *Catal. Today*, 2017, **295**, 110–118.
13 Â. Silva, K. Wilson, A. F. Lee, V. C. dos Santos, A. C. Cons Bacilla, K. M. Mantovani and S. Nakagaki, $Nb_2O_5$/SBA-15 catalyzed propanoic acid esterification, *Appl. Catal., B*, 2017, **205**, 498–504.
14 K. Nakajima, Y. Baba, R. Noma, M. Kitano, J. N. Kondo, S. Hayashi and M. Hara, $Nb_2O_5{\cdot}nH_2O$ as a Heterogeneous Catalyst with Water-Tolerant Lewis Acid Sites, *J. Am. Chem. Soc.*, 2011, **133**(12), 4224–4227.
15 Y. Zhang, J. Wang, X. Li, X. Liu, Y. Xia, B. Hu, G. Lu and Y. Wang, Direct conversion of biomass-derived carbohydrates to 5-hydroxymethylfurural over water-tolerant niobium-based catalysts, *Fuel*, 2015, **139**, 301–307.
16 S. Jin, Z. Xiao, X. Chen, L. Wang, J. Guo, M. Zhang and C. Liang, Cleavage of Lignin-Derived 4-O-5 Aryl Ethers over Nickel Nanoparticles Supported on Niobic Acid-Activated Carbon Composites, *Ind. Eng. Chem. Res.*, 2015, **54**(8), 2302–2310.
17 H. N. Pham, Y. J. Pagan-Torres, J. C. Serrano-Ruiz, D. Wang, J. A. Dumesic and A. K. Datye, Improved hydrothermal stability of niobia-supported Pd catalysts, *Appl. Catal., A*, 2011, **397**(1), 153–162.
18 C. Ramírez-Márquez, J. G. Segovia-Hernández and S. S. Mansouri, 8 - Alcohol production process design and scale-up, in *Higher Alcohols Production Platforms*, ed. H. Amiri, M. Tabatabaei and A.-S. Nizami, Academic Press, 2024, pp. 237–269.
19 M. Mascal, Chemicals from biobutanol: technologies and markets, *Biofuels, Bioprod. Biorefin.*, 2012, **6**(4), 483–493.
20 G. W. Huber, S. Iborra and A. Corma, Synthesis of Transportation Fuels from Biomass: Chemistry, Catalysts, and Engineering, *Chem. Rev.*, 2006, **106**(9), 4044–4098.
21 P. Cavelius, S. Engelhart-Straub, N. Mehlmer, J. Lercher, D. Awad and T. Brück, The potential of biofuels from first to fourth generation, *PLoS Biol.*, 2023, **21**(3), e3002063.
22 L. Pinaeva and A. Noskov, Potentials of bio-butanol conversion to valuable products, *Rev. Chem. Eng.*, 2023, **39**(4), 669–706.
23 V. C. S. Palla, D. Shee and S. K. Maity, Conversion of n-butanol to gasoline range hydrocarbons, butylenes and aromatics, *Appl. Catal., A*, 2016, **526**, 28–36.
24 G. Hayes, M. Laurel, D. MacKinnon, T. Zhao, H. A. Houck and C. R. Becer, Polymers without Petrochemicals: Sustainable Routes to Conventional Monomers, *Chem. Rev.*, 2023, **123**(5), 2609–2734.
25 M. V. Aristizábal, V. C. A. García and A. C. A. Cardona, Integrated Production of Different Types of Bioenergy from

Oil Palm Through Biorefinery Concept, *Waste Biomass Valorization*, 2016, **7**(4), 737–745.

26 S. Geleynse, K. Brandt, M. Garcia-Perez, M. Wolcott and X. Zhang, The Alcohol-to-Jet Conversion Pathway for Drop-In Biofuels: Techno-Economic Evaluation, *ChemSusChem*, 2018, **11**(21), 3728–3741.

27 R. Zhang, Y. He, Y. Luo, D. Lou, R. Zhu, C. Zhu and Q. Li, Selective preparation of jet fuels from low carbon alcohols and ABE at atmospheric pressure, *Energy*, 2023, **281**, 128246.

28 M. Kang, J. F. DeWilde and A. Bhan, Kinetics and Mechanism of Alcohol Dehydration on $\gamma$-$Al_2O_3$: Effects of Carbon Chain Length and Substitution, *ACS Catal.*, 2014, **5**(2), 602–612.

29 S. Roy, G. Mpourmpakis, D.-Y. Hong, D. G. Vlachos, A. Bhan and R. J. Gorte, Mechanistic Study of Alcohol Dehydration on $\gamma$-$Al_2O_3$, *ACS Catal.*, 2012, **2**(9), 1846–1853.

30 S. Nahreen and R. B. Gupta, Conversion of the Acetone–Butanol–Ethanol (ABE) Mixture to Hydrocarbons by Catalytic Dehydration, *Energy Fuels*, 2013, **27**(4), 2116–2125.

31 D. Gunst, K. Alexopoulos, K. Van Der Borght, M. John, V. Galvita, M.-F. Reyniers and A. Verberckmoes, Study of butanol conversion to butenes over H-ZSM-5: Effect of chemical structure on activity, selectivity and reaction pathways, *Appl. Catal., A*, 2017, **539**, 1–12.

32 M. John, K. Alexopoulos, M.-F. Reyniers and G. B. Marin, Reaction path analysis for 1-butanol dehydration in H-ZSM-5 zeolite: Ab initio and microkinetic modeling, *J. Catal.*, 2015, **330**, 28–45.

33 M. John, K. Alexopoulos, M.-F. Reyniers and G. B. Marin, First-Principles Kinetic Study on the Effect of the Zeolite Framework on 1-Butanol Dehydration, *ACS Catal.*, 2016, **6**(7), 4081–4094.

34 M. John, K. Alexopoulos, M.-F. Reyniers and G. B. Marin, Effect of zeolite confinement on the conversion of 1-butanol to butene isomers: mechanistic insights from DFT based microkinetic modelling, *Catal. Sci. Technol.*, 2017, **7**(14), 2978–2997.

35 M. John, K. Alexopoulos, M.-F. Reyniers and G. B. Marin, Mechanistic insights into the formation of butene isomers from 1-butanol in H-ZSM-5: DFT based microkinetic modelling, *Catal. Sci. Technol.*, 2017, **7**(5), 1055–1072.

36 M. A. Makarova, E. A. Paukshtis, J. M. Thomas, C. Williams and K. I. Zamaraev, Dehydration of n-Butanol on Zeolite H-ZSM-5 and Amorphous Aluminosilicate: Detailed Mechanistic Study and the Effect of Pore Confinement, *J. Catal.*, 1994, **149**(1), 36–51.

37 C. P. Nash, A. Ramanathan, D. A. Ruddy, M. Behl, E. Gjersing, M. Griffin, H. Zhu, B. Subramaniam, J. A. Schaidle and J. E. Hensley, Mixed alcohol dehydration over Brønsted and Lewis acidic catalysts, *Appl. Catal., A*, 2016, **510**, 110–124.

38 Z. Buniazet, C. Lorentz, A. Cabiac, S. Maury and S. Loridant, Supported oxides catalysts for the dehydration of isobutanol into butenes: Relationships between acidic and catalytic properties, *Mol. Catal.*, 2018, **451**, 143–152.

39 J. Wu, H.-J. Liu, X. Yan, Y.-J. Zhou, Z.-N. Lin, S. Mi, K.-K. Cheng and J.-A. Zhang, Efficient Catalytic Dehydration of High-Concentration 1-Butanol with Zn-Mn-Co Modified $\gamma$-$Al_2O_3$ in Jet Fuel Production, *Catalysts*, 2019, **9**(1), 93.

40 C. P. Nash, A. Ramanathan, D. A. Ruddy, M. Behl, E. Gjersing, M. Griffin, H. Zhu, B. Subramaniam, J. A. Schaidle and J. E. Hensley, Mixed alcohol dehydration over Brønsted and Lewis acidic catalysts, *Appl. Catal., A*, 2016, **510**, 110–124.

41 E. Hong, H.-I. Sim and C.-H. Shin, The effect of Brønsted acidity of $WO_3$ /$ZrO_2$ catalysts in dehydration reactions of C3 and C4 alcohols, *Chem. Eng. J.*, 2016, **292**, 156–162.

42 V. C. S. Palla, D. Shee and S. K. Maity, Conversion of n-butanol to gasoline range hydrocarbons, butylenes and aromatics, *Appl. Catal., A*, 2016, **526**, 28–36.

43 S. T. Sie, Consequences of catalyst deactivation for process design and operation, *Appl. Catal., A*, 2001, **212**(1), 129–151.

44 F. Wang, H. Z. Wu, C. L. Liu, R. Z. Yang and W. S. Dong, Catalytic dehydration of fructose to 5-hydroxymethylfurfural over $Nb_2O_5$ catalyst in organic solvent, *Carbohydr. Res.*, 2013, **368**, 78–83.

45 N. R. M. Sturt, J. C. S. Terra, D. Lara Sangiorge, L. C. A. Oliveira and F. C. C. Moura, Performance of niobium catalysts in a one-pot system for selective methanol conversion to dimethoxymethane under mild conditions, *Fuel*, 2020, **262**, 116417.

46 T. Kitano, T. Shishido, K. Teramura and T. Tanaka, Characterization of thermally stable Bronsted acid sites on alumina-supported niobium oxide after calcination at high temperatures, *ChemPhysChem*, 2013, **14**(11), 2560–2569.

47 S. H. Lima, A. M. S. Forrester, L. Amparo Palacio and A. C. Faro, Niobia-alumina as methanol dehydration component in mixed catalyst systems for dimethyl ether production from syngas, *Appl. Catal., A*, 2014, **488**, 19–27.

48 M. Abdelrehim, A. Dossantos, V. Camorim and A. Dacostafarojr, Acid–base reactions on alumina-supported niobia, *Appl. Catal., A*, 2006, **305**(2), 211–218.

49 J. M. Conesa, M. V. Morales, N. García-Bosch, I. R. Ramos and A. Guerrero-Ruiz, Graphite supported heteropolyacid as a regenerable catalyst in the dehydration of 1-butanol to butenes, *Catal. Today*, 2023, **420**, 114017.

50 R. Turco, A. Aronne, P. Carniti, A. Gervasini, L. Minieri, P. Pernice, R. Tesser, R. Vitiello and M. Di Serio, Influence of preparation methods and structure of niobium oxide-based catalysts in the epoxidation reaction, *Catal. Today*, 2015, **254**, 99–103.

51 T. Tsuchida and Y. Azuma, Synthesis of niobium carbide and nitride in air from mechanically activated Nb–C powder mixtures, *J. Mater. Chem.*, 1997, **7**(11), 2265–2268.

52 V. L. S. Teixeira da Silva, M. Schmal and S. T. Oyama, Niobium Carbide Synthesis from Niobium Oxide: Study of the Synthesis Conditions, Kinetics, and Solid-State Transformation Mechanism, *J. Solid State Chem.*, 1996, **123**(1), 168–182.

53 A. Gupta, M. Mittal, M. K. Singh, S. L. Suib and O. P. Pandey, Low temperature synthesis of NbC/C nano-composites as visible light photoactive catalyst, *Sci. Rep.*, 2018, **8**(1), 13597.

 

54 A. Prudnikava, Y. Tamashevich, S. Babenkov, A. Makarova, D. Smirnov, V. Aristov, O. Molodtsova, O. Kugeler, J. Viefhaus and B. Foster, Systematic study of niobium thermal treatments for superconducting radio frequency cavities employing X-ray photoelectron spectroscopy, *Supercond. Sci. Technol.*, 2022, **35**(6), 065019.

55 S. A. Chambers, Y. Gao, S. Thevuthasan, Y. Liang, N. R. Shivaparan and R. J. Smith, Molecular beam epitaxial growth and characterization of mixed $(Ti,Nb)O_2$ rutile films on $TiO_2(100)$, *J. Vac. Sci. Technol., A*, 1996, **14**(3), 1387–1394.

56 C. Lang, J. Schnee, B. J. T. Mba, F. Devred and E. M. Gaigneaux, Ammonium-substitution for successfully activating the bulk of Keggin acid salts in 1-butanol dehydration, *Catal. Sci. Technol.*, 2020, **10**(18), 6244–6256.

57 K. Hauge, E. Bergene, D. Chen, G. R. Fredriksen and A. Holmen, Oligomerization of isobutene over solid acid catalysts, *Catal. Today*, 2005, **100**(3–4), 463–466.

58 F. Yi, M. Xing, J. P. Cao, S. Guo and Y. Yang, Comparison of Brønsted Acidic Silanol Nests and Lewis Acidic Metal Sites in Ti-Beta Zeolites for Conversion of Butenes, *Catalysts*, 2024, **14**(11), 749–761.